Characterization of Various Phases of Ice on the Basis of the Charge Density

S. Jenkins and I. Morrison*

Joule Physics Laboratory, School of Sciences, University of Salford, Salford M5 4WT, U.K.

Received: July 28, 1999; In Final Form: October 1, 1999

The many different intermolecular bonding interactions present in seven of the phases of water ice representing a large portion of the phase diagram are systematically examined using the theory of "atoms in molecules" (AIM), we obtain the total charge density distributions calculated using the generalized gradient approximation (GGA) and norm-conserving pseudopotentials. With this approach, we follow the changing properties of the intermolecular bonding from the low- to high-pressure phases of ice, examining ice Ic, ice Ih, ice IX, ice II, ice VI, ice VII, and ice VIII and various proton orderings within these phases. We quantify and characterize not only the familiar hydrogen bonds but also some novel intermolecular O···O bonding interactions, enhancing the understanding of bonding in ice and allowing a more complete explanation of the unusually high number of distinct phases of ice. We also quantify the relative compressibility of the structural features and the bond path rigidity in these ice phases, which have consequences for the mechanisms involved in phase transformations.

1. Introduction

Ice[1] has the unusual property of having many polymorphs (not less than 11 stable or metastable phases have been found to date) which exhibit a wide variety of bonding interactions between distinct water molecules. In all of the phases of ice in this study, four hydrogen bonds surround each water molecule, where two "attach" themselves to the two hydrogens and the other two to the lone pairs on the oxygen atom. The distribution of charge within a water molecule is such that at low pressures it is energetically favorable for ice to form very open structures with approximately tetrahedrally coordinated water molecules. At intermediate pressures, complex structures with large unit cells form where a wide range of hydrogen bond geometries are observed. At high pressures, the equilibrium structures consist of interpenetrating near-tetrahedrally coordinated networks of hydrogen bonds.

Hydrogen bonding plays an important role in determining the structure and properties of a diverse range of inorganic and organic substances. For example, the making and breaking of hydrogen bonds between water molecules and other molecules determine, among other things, reaction pathways in organic and biological systems. A definition of what constitutes a hydrogen bond beyond its geometry is notoriously difficult. A clear description of hydrogen bonding is necessary in any discussion of molecular and crystalline stability, where a quantitative description must be able to follow the effects of changing environments on the hydrogen bond. It has also been realized for some time that ice VIII, a high-pressure phase of ice, has infrared Raman modes where the ice Ic-like sublattices[2] move as rigid units. Later computational work[3] confirms this result and further shows these modes to also exist for ice VII and ice VI. As a direct consequence of this, we were prompted to inquire further into the nature of the bonding interactions between these sublattices. This also prompted a search for intermolecular interactions in ice IX and ice II, distinct from

hydrogen bonds, that assist the hydrogen bonds in stabilizing these very distorted structures.

To construct a unified account of the intermolecular bonding in ice, we have adopted the theory of "atoms in molecules" (AIM).[4] This powerful yet accessible theory allows us to examine the intermolecular bonding in terms of the topology of the total charge density distribution. The AIM method is equally applicable to total charge density distributions derived from experiment or calculated from a theoretical model; we have used the latter method to provide data for analysis. All calculations were performed within the generalized gradient approximation (GGA) to density functional theory using the ab initio pseudopotential method as implemented in the CASTEP code.[5] In this approach Kohn–Sham states and the charge density are obtained as plane wave expansions. This level of approximation is known to reproduce well the energetics of hydrogen bonding.[6] The structure of the paper is as follows. Section 2 (together with accompanying figures) contains a concise account of the geometry of all of the ice phases studied in this work. In section 3, we briefly outline the AIM concepts used in this work and details of our implementation of the method. In this section, we examine not only the familiar hydrogen bonds[7] but also describe and quantify the novel intermolecular O···O interactions using some of the same techniques, as well as applying AIM-based criteria to describe the relative compressibilities of the phases and rigidity of the bond paths. The results of our application of AIM to these phases, using a number of charge density based criteria to allow a systematic examination of the characteristics of intermolecular bonding, are given in section 4. In section 5, we present our conclusions.

2. Geometry

All the phases of ice in this study obey the Bernal–Fowler ice rules[8] in that only one hydrogen exists at approximately one-third of the way between the hydrogen bonded oxygens.

The phases of ice considered in the study are the following: the low-pressure phases ice Ic and ice Ih; the three intermediate-pressure phases ice IX; ice II and ice VI; and the high-pressure

* Corresponding author. Fax: +44 161 295 5903. Phone: +44 161 295 5303. E-mail: I.Morrison@salford.ac.uk.

TABLE 1: Selected Calculated Distances (Angstrom) for the O−H and O−O Interactions for Ice Ic (Three Proton Orderings), Ice Ih (Five Proton Orderings), Ice IX, Ice II, Ice VI, Ice VII, and Ice VIII[a]

Low-Pressure Phases					
ice Ic			ice Ih		
(1)	D O4−H10	1.6933	(1)	A O3−H12	1.6934
(2)	C O−H	1.6938		B O5−H22	1.6919
	D O−H	1.6839		C O6−H23	1.6942
(3)	C O−H	1.6930		D O6−H19	1.6906
			(2)	A O−H	1.6955
			(3)	B O−H	1.6931
			(4)	C O−H	1.6911
			(5)	D O−H	1.6925

Intermediate-Pressure Phases					
ice IX		ice II		ice VI	
O7−H21	1.7186	O5−H25	1.7490	O10−H25	1.8182
O3−H28	1.7546	O6−H31	1.7533	O8−H21	1.8002
O10−H22	1.7708	O10−H14	1.8052	O8−H28	1.8238
O1···O12	3.8350	O11−H24	1.8228	O7−H27	1.8638
O3···O12	3.8496	O2···O7	3.3547	O3−H12	1.8349
O2···O10	3.8514	O6···O12	3.3653	O4···O9	3.4286
O2···O6	3.9598	O5···O11	3.4032	O2···O10	3.4527
		O10···O12	3.5828	O3···O9	3.5084
				O2···O7	3.5105
				O4···O6	3.5256
				O3···O7	3.5274
				O3···O6	3.5647
				O5···O8	3.6503

High-Pressure Phases				
ice VIII		ice VII		
D O8−H26	2.0125	D O−H		1.9583
E O2···O9	2.8695	C O−H		1.9889
F O6···O10	3.1383	E O···O		2.8340
G O3···O16	3.3004	G O···O		3.2606
H O3···O9	3.4356	O···O		3.3846
G* O5···O9	3.7575	H O···O		3.3928
		G* O···O		3.5958

[a] Figure 1d shows the four possible local arrangements of the hydrogen bond represented by A, B, C, and D in this table in the tetrahedrally coordinated phases; see Figure 1a for ice Ic(1), Figure 1b for ice Ih(1), and Figure 1c for ice VIII. For ice IX, ice II, and ice VI, see parts e, f, and g of Figure 1, respectively

phases ice VII and ice VIII. These seven phases of ice show a wide variety of hydrogen bond environments including five-, six-, and eight-membered rings as well as a square helix. We chose to examine representative sets of O···O interactions and hydrogen bonds. These bond geometries are displayed in Figure 1, where parts a−c of Figure 1 inclusive represent the phases with close to tetrahedral coordination and parts e−g of Figure 1 inclusive represent the more distorted phases. The numbering schemes for the molecular interactions considerations are shown in Table 1.

Ice Ic, ice Ih, and ice VII are proton-disordered phases. These structures are modeled within a supercell approach. We present results from three out of four possible proton orderings for an eight-molecule ice Ic unit cell and five out of a possible 17 proton orderings for an eight-molecule ice Ih unit cell.[9] Particular structures can label these different arrangements in terms of the relative orientation of hydrogen-bonded pairs of molecules. There are four possible arrangements[10] which are denoted A, B, C and D as shown in Figure 1d. Ice Ic can only have C- and/or D-type hydrogen bonds, whereas ice Ih can have all four types.

Ice VI, ice VII, and ice VIII all have structures that are composed of sublattices. Each sublattice contains half the total

number of molecules and forms a hydrogen-bonded unit that is *not* hydrogen-bonded to its partner sublattice. Ice VII and ice VIII can be regarded as consisting of two such interpenetrating ice Ic-like sublattices.

For the O···O interactions in ice VII and ice VIII we chose to assign labels E, F, G, H (where H does *not* refer to a hydrogen bond), and G* to particular relative orientations of water molecules (see Figure 1c).

3. Method

3.1. Atoms in Molecules. AIM is an extension of quantum mechanics to subdomains which defines an atom as an open system[4] and provides a uniquely powerful method for the study of bonding using only the charge density distribution $\rho(\mathbf{r})$. We can identify *critical points* in the charge density distribution where $\nabla\rho(\mathbf{r}) = 0$, and further classify these points according to the properties of the Hessian matrix (the matrix of partial second derivatives of $\rho(\mathbf{r})$ with respect to the components of $\mathbf{r}$) evaluated at these points. Diagonalizing this matrix gives the coordinate invariant (ordered) eigenvalues $\lambda_1 < \lambda_2 < \lambda_3$, and the critical points are conventionally labeled using the notation (ω,σ) where ω is the *rank* (the number of distinct eigenvalues) and σ is the *signature* (the algebraic sum of the signs of the eigenvalues). In three dimensions, there are four types of stable critical points; these are denoted as $(3,-3)$ [a local maximum, usually corresponding to a nuclear position], $(3,-1)$ and $(3,+1)$ [saddle points, called *bond critical points* (BCP) and *ring critical points* (RCP), respectively], and $(3,+3)$ [*cage critical points* (CCP)]. We also define a piecewise continuous *gradient path* by evaluating $\nabla\rho$ at some point, then following this vector for an extremely small distance and evaluating $\nabla\rho$ again. In the limit of an infinitely small step, the path is continuous and corresponds to the true gradient path. The pair of special gradient paths linking a BCP with two nuclei and along which ρ is a maximum with respect to any neighboring path is known as an *atomic interaction line* (AIL). A *bond path* is then said to exist between two nuclei linked by an AIL when the forces on the nuclei vanish (i.e., the structure is in equilibrium or geometrically optimized). AIM therefore provides a universal definition of what constitutes a bond—if a bond path exists between two nuclei, they are considered to be bonded. Bond paths are usually linear, corresponding to the traditional definition of a bond, but in electron-deficient structures and/or easily ruptured bonds, they may be significantly curved.

We are particularly interested in properties evaluated at the BCPs, RCPs, and CCPs, e.g., the charge density evaluated at the BCP denoted by ρ_b and the Laplacian $\nabla^2\rho_b$ also evaluated at the BCP. *Closed shell interactions* (e.g., ionic bonds and hydrogen bonds) are characterized by positive values of $\nabla^2\rho_b$, low ρ_b values (<0.1 atomic units), and values of $|\lambda_1|/\lambda_3 < 1$; these types of interactions are dominated by the contraction of charge away from the BCP toward each of the nuclei. Conversely, *shared interactions* (e.g., covalent bonds) have negative $\nabla^2\rho_b$ values, high values of ρ_b, and values of $|\lambda_1|/\lambda_3 > 1$. We can also define an ellipticity $\epsilon = \lambda_1/\lambda_2 - 1$, as a measure of the relative accumulation of charge in the two directions perpendicular to the bond path at a BCP.[4] In section 4, we use these quantities to characterize the bonding interactions.

3.2. Implementation. All previous work on AIM has been performed on geometries obtained using localized basis sets. This work uses a plane-wave basis set, and replaces the oxygen core using a norm-conserving pseudopotential. The properties of this pseudopotential are such that we define only one $(3,-3)$ critical point per molecule. This, however, allows us to set $n =$
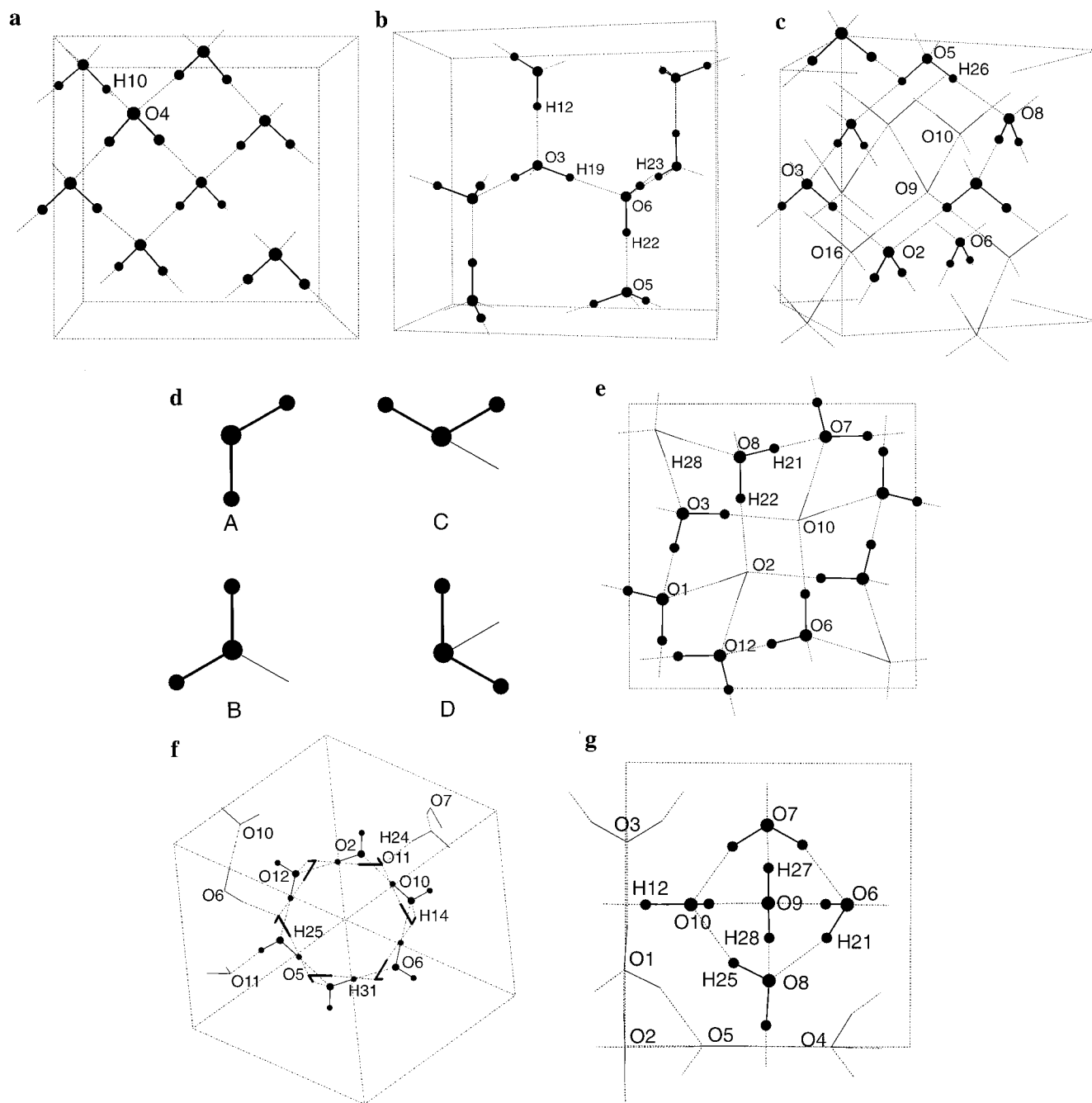
Characterization of Various Phases of Ice

J. Phys. Chem. B, Vol. 103, No. 50, 1999 **11043**

Figure 1. (a) Ice Ic. This low-pressure phase consists of a diamond lattice with a basis of two oxygens, at 0,0,0 and $^1/_4,^1/_4,^1/_4$. Each water molecule has the same geometry. The orientation of the molecules is disordered within the Bernal−Fowler ice rules. The structural disorder is modeled within the eight molecule supercells containing a representative selection of the possible local orientations of the water molecules. (b) Ice Ih. This low-pressure phase consists of a wurtzite structure of eight water molecules. This low-pressure phase is the common phase of ice. Oxygen atoms form a wurtzite lattice. The orientation of molecules is disordered within the Bernal−Fowler ice rules. The structural disorder is modeled within the eight molecule supercells containing a representative selection of the possible orientations of water molecules. (c) Ice VIII viewed parallel to the *c*-axis. The structure consists of two interpenetrating ice Ic lattices that are not hydrogen bonded to each other. These sublattices are oppositely polarized so that ice VIII has zero net polarization. Ice VII is the proton disordered version of ice VIII, and has a cubic unit cell. We model the effect of proton disordering within 16 molecule supercells containing C and D type hydrogen bonds such that the net dipole moment of the cell is zero. (d) The local geometrical arrangement of water molecules associated with the four different geometries of hydrogen bond possible in ice Ic, ice Ih, ice VII, and ice VIII are shown in orthographic projection. The hydrogen bond is normal to the page. The first molecule is shown using filled circles to represent the atoms, and the second molecule is 'behind' the first and is represented as a bent stick so that the hydrogen atom that determines the orientation is clearly shown. (e) Ice IX viewed along the tetragonal *c*-axis. There are two types of water molecules: type I ("ball-and-stick" representation) and type II ("bent cylinder" representation). Molecules of type I form square helical chains around the 4_1-axes parallel to the *c*-axis. The helices are linked laterally by molecules of type II. These are visible as the squares that cross the edges of the unit cell. If the protons were disordered, the structure would be ice III. (f) Ice II viewed down the hexagonal *c*-axis. There are two nonequivalent types of hexagonal ring present in ice II: molecules of type I are shown using "ball-and-stick" representation and those of type II using "bent cylinder" representation. These rings are stacked alternately along the *c*-axis and are linked into columns by hydrogen bonds in the same way as in ice Ih. The protons are in an ordered arrangement, there is no stable proton-disordered form. In the transition of ice Ih to ice II, half of the hexagonal rings are collapsed (compare with ice IX). Three such collapsed hexagonal rings are visible, wrapping around the columns down the *c*-axis. (g) Ice VI viewed along the *c*-axis of the crystal. The molecules are in two parallel hydrogen-bonded sublattices. The positions of the protons are such that the sublattices have equal but opposite polarization, giving zero net polarization and antiferroelectric ordering of the crystal.
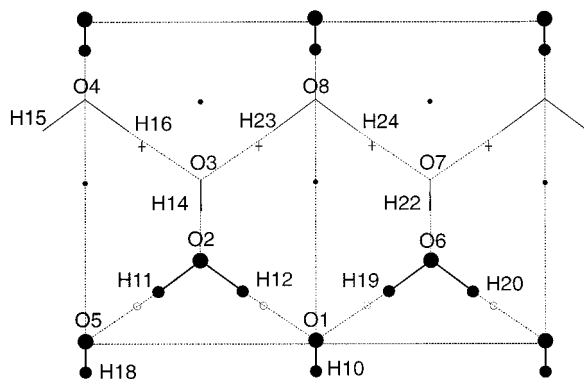
Figure 2. Location of the critical points in the (110) plane of the ice Ic unit cell. The bond, cage, and ring critical points are denoted by circles, crosses and dots, respectively. The projections of the out-of-plane atoms and bond lines are shown by dashes and only the water molecules belonging to the periodic unit cell are numbered.

1, where n is the number of $(3,-3)$ critical points, for each molecule and concentrate on the more interesting intermolecular bonds. Since the ice structures are represented by periodic unit cells, the numbers of critical points are related by a fundamental theorem of topology, the Euler−Poincare relationship.[11]

$$n - b + r - c = 0 \qquad (1)$$

b, r, and c are the numbers of BCPs, RCPs, and CCPs, respectively. We can use this relationship to check that we have found all of the critical points.

We adopted the strategy of first finding all of the RCPs and CCPs. This was achieved by calculating $|\nabla\rho|$ as defined on the points of the real space grid used in the calculation, then displaying an iso-surface corresponding to low values of $|\nabla\rho|$. Regions enclosed by small closed iso-surfaces were identified by inspection, using knowledge of the symmetry of the structure. Taking starting positions inside each of these candidate regions, we iterated toward the location of each true critical point in turn using a general three-dimensional Newton−Raphson search method, calculating the Hessian matrix **H** and $\nabla\rho$ at each step analytically from the plane wave expansion of ρ. All of the AIM features were then derived from the calculated charge densities using a specially developed suite of FORTRAN programs. The topology of the charge density as calculated at the critical points was found to be invariant with respect to shifts through the real space grid. The expression for the step vector $\Delta\mathbf{r}$ used in the search is given by

$$\Delta\mathbf{r} = -\mathbf{H}^{-1}(\mathbf{r}) \cdot \nabla\rho(\mathbf{r}) \qquad (2)$$

the next point being generated by adding the step onto the current point **r**. This process was repeated until $|\nabla\rho|$ fell below a chosen very small threshold value (typically 10^{-10}). Knowing the number and locations of the n $(3,-3)$ points, we then searched for the intermolecular BCPs. For the hydrogen bonds, examination of planes in the charge density map along the hydrogen bond revealed that a good starting point for the Newton−Raphson search was about 30−35% of the way from a hydrogen to its hydrogen-bonded oxygen atom. This method also revealed that good starting points for finding the O···O BCPs lay halfway between the corresponding oxygen atoms. Figure 2 shows the location of the bond, ring, and cage critical points in the (110) plane of ice Ic. Having found all the critical points and evaluated their local properties, we then mapped out the bond paths from each BCP. This was done taking discrete steps out from the BCP along the direction associated with the
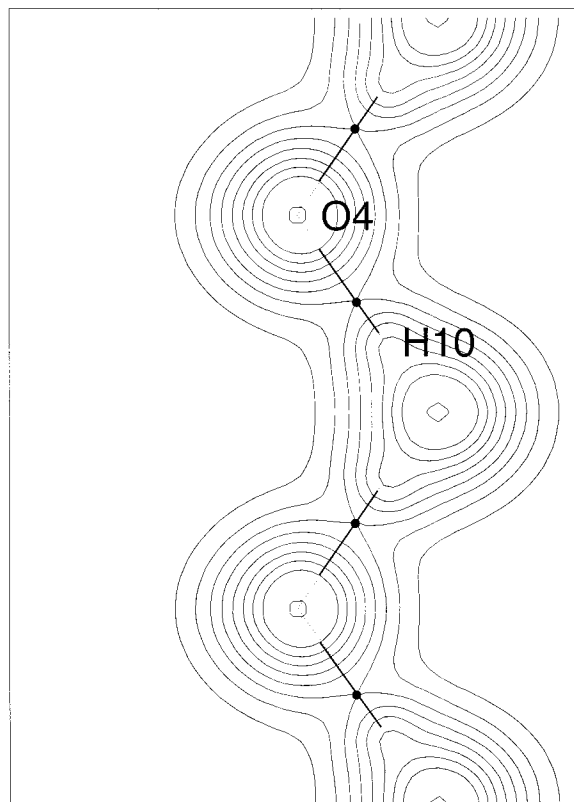

Figure 3. Superposition of the contour lines of the charge density with the molecular graphs of ice Ic. BCPs are shown as dots. The bold solid line represents the extent of the calculated bond path.

λ_3 eigenvalue in both the positive and negative senses, evaluating this direction at each step, then moving a small distance along this direction to generate the next point out along the path. The step size was chosen such that decreasing the step size did not yield a significant change in the calculated bond path length (evaluated as the sum of the step lengths). The total bond path length was then obtained by adding to this the distances from the points at each end of the path where the λ_3 eigenvalue changes sign to the appropriate atom positions. This was done since beyond this point the charge density obtained with the oxygen pseudopotential is increasingly different from the true total charge density. No significant deviation of a bond path from straight line has been observed in all-electron calculations for distances this close to the nuclei. An example bond path in ice Ic is shown in Figure 3.

4. Results and Discussion

We now apply AIM to the problem of systematically describing and quantifying the range of intermolecular bonding interactions using the criteria proposed by Koch and Popelier[7] as a framework. Criteria 5 for the hydrogen bond BCPs and the O···O BCPs is not one of the criteria of Koch and Popelier.

In Section 4.1, we apply these criteria to hydrogen bonds, and in section 4.2, we apply a subset of the criteria to examine the O···O interactions. We further examine the structural properties of the studied phases using two further AIM-derived quantities in section 4.3.

The numbers (satisfying eq 1) and types of critical points found in all of the phases are summarized in Table 2. In Table 2, the number of BCPs has been split into two terms, b_{O-H} and b_{O--O}, to distinguish between the contributions to b from hydrogen bonds and O···O interactions. Note that the low-pressure ice phases, ice Ic and ice Ih, do not possess O···O

TABLE 2: Critical Point Set of Various Phases of Ice (See Text for the Symbols Used Denoting the Types of Critical Points)^a

ice phase	n	b_{O-H}	b_{O--O}	r	c
ice Ic	8	16	0	16	8
ice Ih	8	16	0	12	4
ice IX	12	24	24	64	28
ice II	12	24	18	60	30
ice VI	10	20	40	80	30
ice VIII	16	32	80	12	32

TABLE 3: Analysis of the Hydrogen Bond Critical Points in Ice Phases Ice Ic, Ice Ih, Ice VII, and Ice VIII

ice phase	interaction	ρ_b	λ_1	λ_2	λ_3	$\nabla^2\rho_b$
ice Ic(1)	C O−H	0.0255	−0.044059	−0.042720	0.126504	0.0397
(2)	D O4−H10	0.0255	−0.043916	−0.043054	0.127026	0.0400
(3)	C O−H	0.0255	−0.044175	−0.042828	0.127026	0.0400
ice Ih(1)	A O3−H12	0.0260	−0.045355	−0.043941	0.131727	0.0412
	B O5−H22	0.0262	−0.044855	−0.043742	0.130309	0.0421
	C O6−H23	0.0262	−0.045136	−0.043975	0.130974	0.0419
	D O6−H19	0.0263	−0.045144	−0.043983	0.131003	0.0425
ice Ih(2)	A O−H	0.0260	−0.044714	−0.043148	0.128849	0.0410
(3)	B O−H	0.0260	−0.044643	−0.043528	0.129675	0.0415
(4)	C O−H	0.0262	−0.045050	−0.043717	0.130560	0.0418
(5)	D O−H	0.0261	−0.044886	−0.043774	0.129949	0.0413
ice VII	D O−H	0.0168	−0.025121	−0.024559	0.078761	0.0291
	C O−H	0.0156	−0.023056	−0.022381	0.076977	0.0315
ice VIII	D O8−H26	0.0152	−0.022203	−0.021727	0.077446	0.0335

TABLE 4: Analysis of the Hydrogen Bond Critical Points in Ice Phases Ice IX, Ice II, and Ice VI

ice phase	interaction	ρ_b	λ_1	λ_2	λ_3	$\nabla^2\rho_b$
ice IX	O7−H21	0.0277	−0.046848	−0.044579	0.137209	0.0458
	O3−H28	0.0249	−0.039266	−0.038781	0.115358	0.0373
	O10−H22	0.0267	−0.043440	−0.042085	0.119586	0.0341
ice II	O5−H25	0.0209	−0.034408	−0.033344	0.096344	0.0286
	O6−H31	0.0180	−0.028417	−0.027048	0.082021	0.0266
	O10−H14	0.0203	−0.033573	−0.031509	0.095133	0.0301
	O11−H24	0.0173	−0.027273	−0.026270	0.075949	0.0224
ice VI	O10−H25	0.0177	−0.028221	−0.027066	0.078811	0.0235
	O8−H21	0.0187	−0.029371	−0.028871	0.082175	0.0239
	O8−H28	0.0176	−0.028086	−0.027158	0.077501	0.0223
	O7−H27	0.0166	−0.025331	−0.024473	0.068816	0.0190
	O3−H12	0.0165	−0.026406	−0.025280	0.076646	0.0250

interactions. All charge-related quantities in the following text have been stated using atomic units. In Tables 3−8, we tabulate the quantities used in AIM to quanify bonding properties.

4.1. Charge-Based Criteria for Hydrogen Bonding. *4.1.1. Topology.* The first necessary condition to prove the existence of hydrogen bonds is the correct topology of the gradient vector field. For the hydrogen bonds, the BCPs are found to be in the correct place (between the hydrogen and oxygen, rather closer to the hydrogen than to the oxygen). The RCPs are found in two planes perpendicular to the bond paths and close to either side of the hydrogen bond BCPs. In the more tetrahedrally coordinated structures ice Ic, ice VII, and ice VIII, each of these planes contains three ring points arranged in an equilateral triangle. If a RCP and a BCP coalesce, they destroy each other, resulting in a ruptured bond and an abrupt change in topology or structure.[4] In Tables 7 and 8, we have denoted the separation between a BCP and the closest RCP by D_{rb}. For the hydrogen bond BCPs of ice Ic, the values of D_{rb} are twice those for ice VIII, although the ellipticities are similar. For ice IX, the values of D_{rb} range from 0.75 to 0.89 Å, reflecting the relative tendency to rupture the hydrogen bonds of this phase. This tendency is even more pronounced in ice II ($D_{rb} = 0.52$ Å for O10−H14) and ice VI ($D_{rb} = 0.59$ Å for O3−H12). Another measure of the effect of the environment on the bonding is given by the

curvature of the bond path.[4] We have quantified this using the deviation δ_{bp}, (the perpendicular distance of the BCP from the line separating the nuclei), a straight bond path having $\delta_{bp} = 0$. For the above-mentioned bonds in ice II and ice VI, the hydrogen bond paths are slightly curved, with values of δ_{bp} of 0.009 Å and 0.02 Å, respectively, again indicating bonds which are likely to rupture.

4.1.2. The Charge Density at the BCP. The calculated values of ρ_b for all of the hydrogen bond BCPs lie in the range predicted in ref 7 for hydrogen bonds (0.002−0.035 au), ranging from 0.015 au in ice VIII (see Table 3) to 0.028 au in ice IX (see Table 4).

4.1.3. The Laplacian of the Charge Density at the BCP. The calculated values are given in Tables 3 and 4. As expected from ref 7, the values are positive and comparable to those in the literature (0.024−0.139 au, allowing for small differences in the basis set), ranging from 0.019 au in the O7−H27 interaction in ice VI to 0.0458 au in the O7−H21 interaction in ice IX.

4.1.4. Mutual Penetration of Hydrogen and Acceptor (Oxygen) Atom. The fourth criterion is based on the mutual penetration of the hydrogen (H) and acceptor atom (O) upon hydrogen bond formation. The penetration is defined as the nonbonded radius minus the bonded radius. The nonbonded radius (r^0_O and r^0_H) is defined as the distance of a nucleus to a given charge density contour in the monomer and is measured in the direction of hydrogen bond formation as seen from the relevant nucleus. A value of 0.001 au for the contour is conventionally used as it gives molecular sizes and atomic diameters in good agreement with gas-phase van der Waals radii.[4] The bonded radius (r_O and r_H) within the context of AIM is defined as the distance from a nucleus to the BCP in question. Bringing the definition of the nonbonded radius into the discussion allows the total penetration $\Delta r_O + \Delta r_H$ (see Table 10) to be separated into contributions from the hydrogen and oxygen atoms, where $\Delta r_O = r^0_O - r_O$ and $\Delta r_H = r^0_H - r_H$.

We observed a strong correlation between the ρ_b and the degree of penetration of adjacent atoms (see Table 3) for all of the phases. Also from Table 10 it can be seen that the penetrations for all of the hydrogen bonds are positive, in agreement with ref 7. According to ref 7, this condition is also a *sufficient* condition for the existence of hydrogen bonds.

4.1.5. Loss of Charge of the Hydrogen Atom. This is quantified by the calculation of the Mulliken charges of the hydrogen and oxygen atoms in the various ice phases. These atomic charges are obtained using the method of Segall et al.[12] by projecting the plane wave states onto a localized basis set (the atomic pseudo-orbitals generated from the pseudopotentials in our calculation) using the projection technique of Sanchez-Portal et al.[13] Summing of the charges in the orbitals associated with each atom gives the atomic charge. In Table 12, the net charge q is given by the sum of the nuclear charge and the electron population of the atom. In the low-pressure phases, it is seen that the charge at the hydrogen atom site increases by 0.038e upon hydrogen bond formation coressponding to a loss of 0.038 electrons from each H site. It was found that the charges of any molecule's atoms add up to a maximum of 0.006e and that the overlap population is low enough for the water molecules to preserve their molecular character. The maximum value of the spilling parameter[12] was found to be an acceptably low 0.005. Another method of quantifying loss of charge can be defined within AIM by the calculation of charge within the "atomic basin".[14] This is numerically challenging and will be an interesting course of further study.

TABLE 5: Analysis of the Oxygen−Oxygen Bond Critical Points in Ice Phases Ice VII and Ice VIII

ice phase	interaction	ρ_b	λ_1	λ_2	λ_3	$\nabla^2\rho_b$
ice VII	E O···O	0.005489	−0.003480	−0.003130	0.043541	0.036932
	G O···O	0.003121	−0.001071	−0.001039	0.011173	0.009063
	O···O	0.002917	−0.000827	−0.000816	0.011746	0.010103
	H O···O	0.002703	−0.000958	−0.000416	0.011836	0.010462
	G* O···O	0.002304	−0.000388	−0.000328	0.012079	0.011362
ice VIII	E O2···O9	0.005195	−0.003442	−0.002496	0.040998	0.035060
	F O6···O10	0.004738	−0.002696	−0.002144	0.017467	0.012627
	G O3···O16	0.003000	−0.001368	−0.001367	0.009663	0.006928
	H O3···O9	0.002705	−0.001001	−0.000693	0.012526	0.010832
	G* O9···O5	0.001820	−0.000386	−0.000386	0.008943	0.008171

TABLE 6: Analysis of the Oxygen−Oxygen Bond Critical Points in Ice Phases in Ice Phases Ice IX, Ice II, and Ice VI

ice phase	interaction	ρ_b	λ_1	λ_2	λ_3	$\nabla^2\rho_b$
ice IX	O1···O12	0.000849	−0.000406	−0.000325	0.002833	0.002102
	O3···O12	0.000845	−0.000282	−0.000209	0.004264	0.003773
	O2···O10	0.000766	−0.000245	−0.000134	0.002468	0.002090
	O2···O6	0.000897	−0.000276	−0.000102	0.003240	0.002862
ice II	O2···O7	0.001365	−0.000784	−0.000558	0.006401	0.005058
	O6···O12	0.001932	−0.001064	−0.000769	0.008043	0.006210
	O5···O11	0.002195	−0.001266	−0.001068	0.007283	0.004949
	O10···O12	0.001335	−0.000722	−0.000625	0.007590	0.006243
ice VI	O4···O9	0.001733	−0.000858	−0.000665	0.007881	0.006358
	O2···O10	0.001867	−0.000951	−0.000676	0.009535	0.007908
	O3···O9	0.001589	−0.000798	−0.000522	0.009004	0.007684
	O2···O7	0.001677	−0.000896	−0.000551	0.009994	0.008547
	O4···O6	0.001218	−0.000664	−0.000331	0.007196	0.006201
	O3···O7	0.001286	−0.000742	−0.000232	0.007354	0.006379
	O3···O6	0.001377	−0.000642	−0.000540	0.008084	0.006901
	O5···O8	0.001427	−0.000556	−0.000306	0.005554	0.004692

TABLE 7: Stability of All the Intermolecular Bond Critical Points in Ice Phases Ice Ic, Ice Ih, Ice VII, and Ice VIII, Where δ_{bp} Is the Perpendicular Distance of the BCP from the Line Separating the Nuclei and D_{rb} Denotes the Separation of a BCP and the Closest RCP to it

ice phase	interaction	$|\lambda_1|/\lambda_3$	ϵ	D_{rb}	δ_{bp}
ice Ic(1)	D O−H	0.3442	0.0203	2.2000	
	C O−H	0.3432	0.0197	2.1899	
(2)	D O4−H10	0.3478	0.0314	2.2185	
(3)	C O−H	0.3478	0.0315	2.1560	
ice Ih(1)	A O3−H12	0.3470	0.0363	2.3760	
	B O5−H22	0.3443	0.0256	2.3752	
	C O6−H23	0.3451	0.0305	2.1309	
	D O6−H19	0.3454	0.0254	2.2752	
ice Ih(2)	A O−H	0.3443	0.0322	2.3394	
(3)	B O−H	0.3443	0.0254	2.4005	
(4)	C O−H	0.3446	0.0264	2.1316	
(5)	D O−H	0.3446	0.0264	2.0576	
ice VII	D O−H	0.3190	0.0229	1.1577	
	C O−H	0.2995	0.0302	1.2485	
	E O···O	0.0799	0.1119	1.0717	
	G O···O	0.0958	0.0303	0.5089	
	O···O	0.0704	0.0129	0.4470	0.0521
	H O···O	0.0809	1.3032	0.4206	0.1011
	*G O···O	0.0322	0.1828	0.1000	0.0736
ice VIII	D O8−H26	0.2866	0.0219	1.1067	
	E O2···O9	0.0840	0.3789	1.0928	
	F O6···O10	0.1544	0.2578	1.1105	
	G O3···O16	0.1415	0.0003	0.4959	
	H O3···O9	0.0799	0.4439	0.4962	
	G* O9···O5	0.0432	0.0005	0.1401	

TABLE 8: Stability of All the Intermolecular Bond Critical Points in Ice Phases Ice IX, Ice II, and Ice VI (See the Table 7 Title for Explanations of δ_{bp} and D_{rb})

ice phase	interaction	$|\lambda_1|/\lambda_3$	ϵ	D_{rb}	δ_{bp}
ice IX	O7−H21	0.3414	0.0509	0.7853	
	O3−H28	0.3404	0.0125	0.7538	
	O10−H22	0.3632	0.0322	0.8917	
	O1···O12	0.1434	0.2492	0.3767	0.4492
	O3···O12	0.0661	0.3484	0.5237	0.1353
	O2···O10	0.0991	0.8272	0.2613	0.4502
	O2···O6	0.0853	1.6992	0.7112	
ice II	O5−H25	0.3571	0.0319	1.7240	
	O6−H31	0.3466	0.0506	1.2249	
	O10−H14	0.3529	0.0655	0.5244	
	O11−H24	0.3591	0.0382	1.2916	
	O2···O7	0.1226	0.4040	0.6602	0.0851
	O6···O12	0.1323	0.3841	0.9560	
	O5···O11	0.1739	0.1858	0.9748	
	O10···O12	0.0951	0.1547	0.3494	
ice VI	O10−H25	0.3581	0.0173	1.0448	
	O8−H21	0.3574	0.0427	1.3703	
	O8−H28	0.3624	0.0342	1.2477	
	O7−H27	0.3681	0.0445	1.4059	
	O3−H12	0.3445	0.0350	0.5939	0.0222
	O4···O9	0.1089	0.2914	0.5332	0.1510
	O2···O10	0.0997	0.4053	0.6290	0.1851
	O3···O9	0.0886	0.5279	0.3526	0.2145
	O2···O7	0.0897	0.6263	0.6278	0.2527
	O4···O6	0.0923	1.0057	0.5220	
	O3···O7	0.1009	2.1932	0.5611	
	O3···O6	0.0795	0.1893	0.3468	0.1484
	O5···O8	0.1002	0.8201	0.1206	0.2185

4.2. The Charge-Based Criteria for Longer Range Interactions. We also applied the criteria proposed in ref 7 to the longer range O···O interactions in five of the phases of ice in this study (ice IX, ice II, ice VI, ice VII, and ice VIII). This is done in order to be able to compare and contrast these new closed shell interactions with the more familar hydrogen bonds. We have found and analyzed O···O bond paths in these structures.

4.2.1. Topology. As a consequence of eq 1 being satisfied, we find BCPs (see Table 1) occurring between pairs of oxygens.

All of O···O BCPs lie approximately midway between the two oxygens connected by a bond path. The phases which possess sublattices (i.e., ice VII, ice VIII, and ice VI) only have O···O BCPs and associated bond paths between sublattices (see Tables 5 and 6). The presence of an O···O bond path is not simply related to the O···O separation (e.g., there is a short intrasublattice O···O separation in ice VI (3.43 Å) which does not have a bond path), also in ice IX and ice II *not all* O···O separations have associated bond paths.

Characterization of Various Phases of Ice

J. Phys. Chem. B, Vol. 103, No. 50, 1999 **11047**

TABLE 9: Trends in the Structural Compressibility of the Ice Phases, Ice Ic, Ice Ih, Ice VII, Ice VIII, Ice IX, Ice II, and Ice VI as Given by $\nabla^2\rho_c$

Low-Pressure Phases		
ice Ic(1)	ice Ic(2)	ice Ih(1)
0.000750	0.000758	0.000295
	0.000812	0.000307
		0.000357
		0.000477

Intermediate-Pressure Phases		
ice IX	ice II	ice VI
0.001402	0.000171	0.001903
0.002127	0.003155	0.004213
0.003167	0.006799	0.008445

High-Pressure Phases	
ice VII	ice VIII
0.009391	0.010141
0.011640	
0.012157	

As in our study of the hydrogen bonds, we found groups of RCPs identifiable with specific O···O BCPs. These occurred in groups of four (two sets of two) around the BCPs. In ice VII and ice VIII, we observed that the four RCPs were almost coplanar, forming a square in the plane perpendicular to the bond path, with the BCP at the center. The low D_{rb} values (0.10 and 0.12 Å for ice VII and ice VIII, respectively) (see Table 7) indicate that these bond paths are close to rupturing; these distances compare well to those previously associated with unstable bonds.[15]

From Table 8, we see that some of these O···O interactions have quite curved bond paths, e.g., in ice IX the O2···O10 bond path is 3% longer than the linear separation of O2 and O10. In this phase, there is a positive correlation between the deviation δ_{bp} of the bond path and D_{rb} for all four of the representative O···O interactions, but this correlation does not hold between D_{rb} and the ellipticities. This is also the case for ice VI. In ice II, only the O2···O7 interaction has a significant deviation associated with its bond path, but this also has the largest ellipticity. Again, there is no good correlation between D_{rb} values and the ellipticity values other than the fact that the ellipticities are all quite high and the D_{rb} values are reasonably small.

For ice VII and ice VIII, the ellipticity of the O···O interactions appears to be a good predictor of the relative

stability of the phases. It has been found for small unit cells (16 molecules for ice VIII and ice VII and 10 molecules for ice VI) that the adiabatic surface around the energy minimum for nonzero total μ (where μ is the molecular dipole moment) is very flat and so the bond paths are more easily prone to distortion.[3] For example, the G and G* O···O interactions in both ice VII and ice VIII are parallel to the direction of total dipole moment of each sublattice and in ice VIII these interactions are *very* nonelliptical (see Table 7). If we examine a variant of the ice VII structure, which is already known to be unstable since it has a total unit cell dipole moment of $32^{1/2}\mu$, the values of ϵ are a lot higher for the G and G* bonds (0.097 and 0.83, respectively) than the equivalent BCPs in the stable forms of ice VII (0.030 and 0.183) and ice VIII (0.0003 and 0.0005). For ice VIII, each sublattice has a total dipole moment of 8μ, compared to a value of 4μ for ice VII. Using this observation, we attribute the very low ellipticities of these bonds in ice VIII as being due to a cooperative polarization effect of the water molecules.

We are currently conducting further investigations into the relationship between the static analysis made possible using AIM (i.e., requiring only one charge density calculation) and previously calculated dynamical properties.

4.2.2. Charge density at the BCP. Typically the O···O interactions in any given phase have a charge density at the BCPs at least an order of magnitude lower than at the hydrogen BCPs. The range of values obtained for the O···O BCPs is 0.0008−0.005 au, compared with 0.015−0.028 au for the hydrogen bond BCPs.

4.2.3. The Laplacian of the Charge Density at the BCP. As expected for a closed shell interaction, these values are positive (see Tables 5 and 6) and range from 0.002 to 0.037 au. The upper end of this range is comparable to the upper end of the range for hydrogen bonds mentioned previously (0.019−0.046 au), but the lower end of the range is an order of magnitude lower. It was observed that the G and G* O···O BCPs in ice VIII have similar values of λ_3 and $\nabla^2\rho_b$ but quite different values of ρ_b. This suggests that a cooperative polarization effect is important in both of these interactions: we show elsewhere[16] that the binding energies of these two interactions are similar.

4.2.4. Mutual Penetration of the Fragments of the O···O Interaction. We calculated the penetrations for the O···O interactions in an analogous way to the hydrogen bonds. Table 11 contains the results for ice VIII. In this phase, the penetrations

TABLE 10: Mutual Penetration of the Monomers (Angstroms) Constituting the Ice Phases Ice Ic, Ice Ih, Ice VII, Ice VIII, Ice IX, Ice II, and Ice VI Where the Monomers Are the Water Molecules

ice phase	interaction	r^0_O	r_O	Δr_O	r^0_H	r_H	Δr_H	$\Delta r_O + \Delta r_H$
ice Ic	O4−H10	1.7003	1.1533	0.5470	1.0881	0.5453	0.5428	1.0898
ice IX	O7−H21	1.7103	1.1593	0.5510	1.1258	0.5593	0.5665	1.1175
	O3−H28	1.6588	1.1796	0.4792	1.1311	0.5752	0.5559	1.0351
	O10−H22	1.7245	1.1877	0.5368	1.1317	0.5829	0.5488	1.0856
ice II	O6−H31	1.7533	1.1792	0.5741	1.0729	0.5742	0.4987	1.0728
	O11−H24	1.6629	1.2154	0.4475	1.0719	0.6073	0.4646	0.9121
ice VI	O8−H28	1.6699	1.2111	0.4588	1.0869	0.6127	0.4742	0.9330
ice VII	O−H	1.7457	1.3010	0.4447	1.1218	0.6893	0.4325	0.8772
ice VIII	O8−H26	1.7501	1.3119	0.4382	1.1295	0.7008	0.4287	0.8669

TABLE 11: Mutual Penetration of the Monomers (Angstroms) Constituting Ice VIII Where the Monomers Are the Water Molecules

ice phase	interaction	r^0_{O1}	r_{O1}	Δr_{O1}	r^0_{O2}	r_{O2}	Δr_{O2}	$\Delta r_{O1} + \Delta r_{O2}$
ice VIII	E O2···O9	1.6455	1.4348	0.2108	1.6455	1.4348	0.2108	0.4215
	F O6···O10	1.8150	1.5692	0.2459	1.8150	1.5692	0.2459	0.4917
	G O3···O16	1.6994	1.6501	0.0493	1.6994	1.6501	0.0493	0.0986
	H O3···O9	1.7807	1.7179	0.0628	1.7807	1.7179	0.0628	0.1256
	G* O5···O9	1.8723	1.8787	−0.0064	1.8723	1.8787	−0.0064	−0.0128

11048 *J. Phys. Chem. B, Vol. 103, No. 50, 1999*

Jenkins and Morrison

TABLE 12: Mulliken Charges of the Oxygens and Hydrogens in the Ice Phases Ice Ic, Ice Ih, Ice VII, Ice VIII, Ice IX, Ice II, and Ice VI

Low-Pressure Phases			
ice Ic		ice Ih(1)	
O	−1.044	O	−1.044
H	0.522	H	0.522
H	0.522	H	0.522
H₂O		ice Ih(2)	
O	−0.967	O	−1.041
H	0.484	H	0.521
H	0.484	H	0.521

Intermediate-Pressure Phases					
ice IX		ice II		ice VI	
O	−1.040	O	−1.051	O	−1.029
H	0.522	H	0.525	H	0.514
H	0.523	H	0.525	H	0.509

High-Pressure Phases			
ice VIII		ice VII	
O	−1.021	O	−1.020
H	0.510	H	0.510
H	0.510	H	0.509
ice VIII(a)[a]			
O	−0.966		
H	0.483		
H	0.483		
ice VIII(b)[b]			
O	−1.030		
H	0.515		
H	0.515		

[a] This refers to the a single water molecule, where charge density was calculated for a single water molecule only in an ice VIII unit cell. [b] This refers to a single (eight molecule) sublattice of ice VIII, where charge density was calculated for a single sublattice of ice VIII only in an ice VIII unit cell.

$\Delta O1$ and $\Delta O2$ are equal for a particular O···O interaction due to the symmetry of the structure. It was seen that all of the O···O interactions except G* satisfy the same sufficient condition as used for the hydrogen bonds, i.e., that the penetrations for both monomers linked by the bond path are positive, thus providing further evidence of the importance of these O···O interactions in ice VIII.

The relationship between depth of penetration and amount of charge at the BCP is not as clear as for the hydrogen bonds; for instance, the monomers of the H-type O···O interaction have a greater penetration than the monomers of the G-type O···O interaction even though there is more charge at the latter BCP (see Table 5). This strongly suggests that the G O···O interaction is weaker that the H O···O interaction. Calculations of the binding energy[16] within an AIM framework confirm this.

Overall, we observed a general tendency for shorter O···O bond paths to have greater total (positive) penetrations than for longer bond paths. This is evidenced in ice IX, where all of the four long representative O···O interactions have negative individual and total penetrations, and in ice II and ice VI, where the O···O interactions possess a mixture of positive and negative penetrations, again corresponding to shorter and longer bond paths, respectively.

4.3. Comparison of the Structural Properties of the Ice Phases. *4.3.1. Compressibility of the Ice Phases.* Features in the charge topology known as cages exist inside closed 3-D

networks of bond paths. In ice Ih and ice Ic, the CCPs are situated at the centers of the structural cages defined by the hydrogen bonding. This is shown in Figure 3 for ice Ic; the positions of the RCPs and CCPs agree with the results of Abramov and Okamura[17] who examined the Laplacian of the charge at the CCPs ($\nabla^2\rho_c$) for diamond-type crystals.

Comparing two CCPs shows that the one with the smaller value of $\nabla^2\rho_c$ corresponds to the more crushable structure. In Table 9, the values of $\nabla^2\rho_c$ for the ice Ic structures show that the cages are much less susceptible to compression than those in the ice Ih structure; we have compared these two phases because they have very similar properties associated with the charge density at their respective BCPs. Evidence for this link is provided by extensive experimental work on ice[1] which shows that it is ice Ih, not ice Ic, which transforms into ice IX and ice II when the pressure is increased.

Ice IX, ice II, and ice VI have a range of different sizes and types of cage, due to the lack of tetrahedral coordination. This is reflected in the range of values of $\nabla^2\rho_c$. For instance, in ice IX, the four weakest (in terms of $\nabla^2\rho_c$) cage points form a square helix inside the central square helix of hydrogen bond BCPs. In ice II, the weakest cage point by far lies at the center of the cylindrical cage structure created between the two types of parallel six-membered rings of molecules which stack alternately along the *c*-axis. This strongly suggests that the cage formed by these rings will collapse before other parts of the structure as the pressure is increased.

4.3.2. The Ratio $|\lambda_1|/\lambda_3$. The ratio $|\lambda_1|/\lambda_3 < 1$ holds for all closed shell interactions. These interactions are dominated by the contraction of charge away from the interatomic surface toward each of the fragments enclosed within their respective zero Laplacian surfaces.

The values of this ratio has been used to compare the range of hydrogen bond environments present in the structures under consideration.

In Tables 7 and 8, we see that, in the low-pressure phases (ice Ic and ice Ih), the values of this ratio for the hydrogen bond BCPs are very consistently ~0.34, demonstrating that this quantity is independent of proton ordering. The intermediate pressure phases ice IX, ice II, and ice VI have some hydrogen bond BCPs with higher values of the ratio, the BCPs with more ice Ic-like values being associated with more unstable hydrogen bond paths as given by the values of ϵ and D_{rb}. As the pressure increases, maintaining bond paths which are more ice Ic-like in this way renders these bond paths increasingly unstable. The high-pressure phases ice VII and ice VIII both have lower values of the ratio than even ice Ic, so the hydrogen bonds are even easier to form than those in the low-pressure phases; these phases instead form interpenetrating tetrahedrally coordinated sublattices.

5. Conclusions

We have demonstrated that AIM is a very powerful method of examining and quantifying intermolecular bonding interactions. A large amount of information can be recovered from the charge density distribution (either generated from a single calculation or obtained from experiment), including predictions of possible mechanisms for structural change. We can also gain an insight into the relative stabilities of different interactions in a particular structure. We have found and quantified the intermolecular O···O interactions in a wide range of structures of ice making up a large portion of the phase diagram. We have shown that the presence or absence of O···O interactions, while having important effects on structural changes and stability, is

Characterization of Various Phases of Ice

J. Phys. Chem. B, Vol. 103, No. 50, 1999 **11049**

not simply dependent on the O⋯O separations; rather, like all bonding interactions, they are features of the global topology of the total charge density distribution.

The findings here infer that in ice V (which was out of the range of our computational resources) there are O⋯O interactions present as a consequence of the very distorted tetrahedral geometry and also that for the representative hydrogen BCPs there will be at least one with a value close to 0.34 for $|\lambda_1|/\lambda_3$, i.e., the value found for the low-pressure phases, and that this will correspond to a particularly unstable hydrogen bond.

We further suggest that AIM could be applied in the future to study the nonmolecular phases ice X and ice XI that have been predicted to exist at very high pressures, ∼3 Mbar.[18] We predict that the bonding interactions in these hypothesized phases will be of the shared shell type. We suggest that the quartzlike polymorph ice XII that has been predicted to exist at pressures under 3−5 kbar and 225−240 K[19] does not possess any O⋯O interactions.

References and Notes

(1) Hobbs, P. V. *Ice Physics*; Clarendon Press: Oxford, 1974.

(2) Wong, P. T. T.; Whalley, E. *J Chem. Phys*. **1976**, *64* (6), 2359−2366.

(3) Jenkins, S.; Morrison, I. Submitted.

(4) Bader, R. F. W. *Atoms in Molecules: A Quantum Theory*; The International Series of Monographs on Chemistry 22; Oxford University Press: New York, 1994.

(5) Payne, M. C.; Teter, M. P.; Allan, D. C.; Arias, T. A.; Joannopoulos, J. D. *Rev. Mod. Phys.* **1993**, *64*, 1045.

(6) Hamann, D. R. *Phys. Rev B* **1997**, *55* (16), 10157−10160.

(7) Koch, U.; Popelier, P. L. A. *J. Phys. Chem*. **1995**, *99*, 24.

(8) Bernal, J. D.; Fowler, R. H. *J. Chem. Phys.* **1933**, *1*, 515.

(9) Howe, R. *J. Phys.* **1987**, *48* (3), 559−563.

(10) Li, J. C.; Ross, D. K. *Nature* **1993**, *365*, 327.

(11) Johnson, C. K.; Burnett, M. N. *Crystallographic Topology and Its Applications*, Proceedings of Macromolecular Crystallography Computing School; Western Washington University, Bellingham, WA, Aug. 17−23, IUCR, 1996.

(12) Segall, M. D.; Pickard, C. J.; Shah, R.; Payne, M. C. *Mol. Phys.* **1996**, *89*, 571.

(13) Sanchez-Portal, D.; Artacho, E.; Soler, J. M. *Solid-State Commun*. **1995**, *95*, 685.

(14) Popelier, P. L. A. *Mol. Phys.* **1996**, *87* (5), 1169−1187.

(15) Popelier, P. L. A.; Bader, R. F. W. *J. Phys. Chem.* **1994**, *98*, 4473−4481.

(16) Jenkins, S.; Morrison, I. To be published.

(17) Abramov, Yu. A.; Okamura, F. P. *Acta Crystallogr.* **1997**, *A53*, 187−198.

(18) Benoit, M.; Bernasconi, M.; Focher, P.; Parrinello, M. *Phys. Rev. Lett.* **1996**, *76* (16), 2934−2936.

(19) Svishchev, I. M.; Kusalik, P. G. *Phys. Rev. B* **1996**, *53* (14), 8815−8817.